Proceedings of ASME Turbo Expo 2011
GT2011
June 6-10, 2011, Vancouver, British Columbia, Canada

GT2011-45555

INFLUENCE OF INLET SWIRL DISTRIBUTIONS ON AN INTER-TURBINE DUCT PART II: HUB SWIRL VARIATION

Yanfeng Zhang, Shuzhen Hu[1], Xue Feng Zhang, **Edward Vlasic**

National Research Council Canada
Ottawa, ON, Canada

Pratt & Whitney Canada
Longueuil, QC, Canada

ABSTRACT

The inter-turbine transition duct (ITD) of a gas turbine engine has significant potential for engine weight reduction and/or aerodynamic performance improvement. This potential arises because very little is understood of the flow behavior in the duct in relation to the hub and casing shapes and the flow entering the duct (e.g., swirl angle, turbulence intensity, periodic unsteadiness and blade tip vortices from upstream HP turbine blade rows). In this study, the flow development in an ITD with different inlet swirl distributions was investigated experimentally and numerically. The current paper, which is the second part of a two-part paper, presents the investigations of the influences of the hub swirl variations on the flow physics of ITD.

The results show that the radial movement of the low momentum hub boundary layer and wake flow induces a pair of hub counter-rotating vortices. This pair of counter-rotating vortices merges with the upstream vorticity, forming a pair of stronger vortices, which persist until ITD exit. Due to the hub streamwise adverse pressure gradient, the hub 3D separation occurs at the exit of the ITD. The hub counter-rotating vortices are strongest with the highest inlet swirl gradient. The hub boundary layer thickness is thickest with the largest inlet hub swirl angle. The hub 3D separation is reduced by the increased hub swirl angle. Based on the studies in both parts of this paper, a detailed loss mechanism has been described. The total pressure coefficient shows that the loss increases gradually at the first bend, and then increases more rapidly at the second bend. The total pressure coefficients within the ITD are significantly redistributed by the casing and hub counter-rotating vortices.

INTRODUCTION

The ITD located between the high-pressure turbine (HPT) and low-pressure turbine (LPT) (shown in Figure 1), is a gas turbine component that has been investigated extensively recently. The design of ITDs is likely to become more aggressive with the demands for lighter, more efficient and environment-friendly aircraft engines. Such aggressive inter-turbine transition ducts (AITD) could have shorter axial length and/or larger HPT-to-LPT radial offset, which contains higher risk of boundary layer separation.

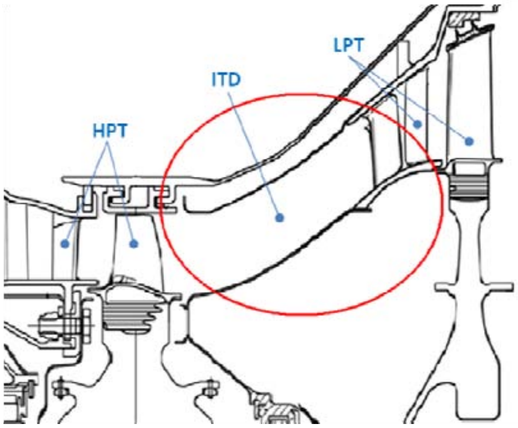

Figure 1. Typical ITD region in a turbofan aeroengine

Hu *et al.* [1] reported that the strong adverse pressure gradient along ITD endwalls caused the boundary layer separation. The endwall static pressure distribution was also significantly influenced by the local curvature distribution. However, if the flow at the entry of an ITD was swirling, the effective local curvature would be reduced by the longer flow path. Furthermore, to balance the centrifugal force, the local effect of swirling produced a radial pressure gradient, which increased the static pressure along the casing and decreased it

---

[1] Ph.D. candidate, Jointly with the Institute of Engineering Thermophysics, Chinese Academy of Sciences.

along the hub. Therefore, to design the AITD with confidence, the inlet swirl influence on the performance of ITD is necessary to be studied in detail.

The swirl influence in a simple diffuser has been well documented by Bradshaw [2]. The investigations of streamline curvature effects on turbulent flow showed that the swirling flow in an annular passage altered the turbulent structure. This different turbulent structure along the casing and the hub implied the variation in the growth rate of the surface boundary layers and their ability to sustain the adverse pressure gradient. Lohmann *et al.* [3] experimentally studied a series of diffusers with various lengths, area ratios and cant angles under a range of inlet swirl angles. The authors pointed out that the tangential component of the flow was independent of the meridional velocity and the angular momentum was conserved despite the variation in the meridional flow. Kumart *et al.* [4] experimentally investigated the effects of the different inlet swirls through an annular diffuser. It was shown that the increase of inlet swirl reduced the likelihood of casing boundary layer separation. It was therefore suggested that the effect of swirl on the diffuser was possibly greater.

In contrast to the basic diffuser geometries, the inlet swirl effects on the flow in the annular S-shaped diffusers have not been investigated extensively, although, in recently years, many researchers were devoted to the investigation of flow development within an ITD.

Miller *et al*. [5] performed measurements downstream of a single-stage transonic HPT stage to examine the migration and dissipation of flow phenomena (e.g., wakes, vortices, etc.) within an ITD. The results obtained in the absence of the LPT vanes showed that two co-rotating streamwise vortices dominate the flow field as the flow approached the inlet plane of the second stage vane. Subsequently, Miller *et al*. [6] carried out the investigation of vane/vortex interaction with a low aspect ratio second stage vane installed within the ITD. Results showed that the structure of secondary flow in the low aspect ratio vane was changed significantly in the presence of the upstream stage. Marn *et al.* [7] and Göttlich *et al.* [8] investigated the influence of the blade tip gap on the performance of a high-diffusion ITD in a transonic turbine test facility. No separation was detected in the duct. It was observed that CFD could capture the influence of changes in tip clearance on flow field behavior. Additionally, the authors found that the tip clearance flow had a significant effect on the duct performance. Furthermore, Marn *et al*. [9] investigated the effect of tip clearance size on the flow in a super-aggressive ITD which is 20% short than the one in Marn *et al.* [7]. Oil flow visualization results showed full separation along the casing for both gaps. Also the authors pointed out the vortices at the casing downstream of the first bend are imposed by the upstream HP vanes.

Dominy and Kirkham [10, 11] and Dominy *et al.* [12] were early investigators of the inlet swirl flow influence in an ITD numerically and experimentally. The authors claimed that the swirl modified the static pressure distribution along the endwalls and enhanced the wake skewness. Although the swirl and the wake did not result in large changes in overall loss, the secondary flow structures and the distribution of losses within the duct were affected significantly. Additionally, the predicted results were compared to the experimental data to test the capability of the CFD. It was found that, with no upstream swirl vanes present, the numerical results were in good agreement with the measurements. With swirl vanes located upstream of the ITD, differences between the measurements and computations were observed near the end-walls. Bailey and Carrotte [13] presented a detailed experimental investigation between "clean" and "swirling" case to determine the inlet swirl effects on the flow with an annular S-shape inter-compressor transition duct. The authors found that the tangential momentum was conserved within the duct and the significant change of streamwise pressure gradient was also detected with the effect of inlet swirling flow. Axelsson *et al.* [14], Axelsson and Johansson [15] conducted experimental investigation of flow development within an ITD in a large scale low-speed facility with an HPT stage upstream. An LPT vane ring was installed downstream of the ITD to simulate real exit boundary conditions. Three different operating conditions of the HPT (*i.e.,* varying the rotor speed) were examined. Results showed the absence of end-wall boundary layer separation in the ITD at both the design and off-design conditions. However, at the off-design condition with large swirl angles, a small region of boundary layer separation was detected on the blade suction surface of the LPT vane. The pressure loss coefficient showed that the lowest happened in the design condition and the highest happened in the larger swirl condition. Zhang *et al.* [16] described how the upstream flow field influenced the flow development in the ITD. The radial movement of the low momentum flow driven by the local radial pressure gradient induced a pair of counter-rotating vortices at the hub region. They also claimed that although the numerical simulation had difficulty in capturing the real boundary layer separation, it came close to capturing the flow physics within ITD.

From the previous work presented above, although the detailed investigation about the inlet swirl influence on the flow development within an ITD had been documented by many researchers, systematic research concerning the effects of inlet swirl has not been conducted yet. The long-term goal of the current project is to parametrically investigate the detailed flow field of modern and aggressive ITDs with upstream HPT stage and downstream LPT vanes as well as the struts inside the ITD. In the current study, the flow development in a modern ITD with different inlet swirl distributions was investigated experimentally and numerically. The different inlet swirl angles are generated by a swirl vane ring located upstream of the ITD. The present papers focus on improving the physical understanding of the swirl influence on the flow field within the ITD.

Five different inlet swirl distributions were generated by five specifically designed vane rings, which can be classified into two sets. The first set is to keep the hub swirl constant (20º) and to vary the casing swirl (20º, 30º & 40º), while the second set is to keep the casing swirl constant (30º) and to vary the hub swirl (10º, 20º & 30º). The current paper, which is the second part of the two-part paper, presents the experimental and numerical investigations of the hub swirl influences on the flow development of the ITD. Furthermore, the loss mechanism within the ITD is described based on the flow physics in all five test cases.

EXPERIMENTAL & NUMERICAL METHODS

The investigation was conducted in a large scale, low-speed, axial turbine facility at the National Research Council Canada. The detailed description of the test facility can be found in Part I of this paper (Hu *et al.* [17]). As shown in Figure 2, a ring of 48 swirl vanes is installed 25 mm upstream of the ITD to provide wakes and swirl to the test section. The ITD test section is an annular test rig with rotatable casing to provide circumferential traverse for measurements. The current test section, ITD Build A, which is representative of a modern engine design, has a duct outlet-to-inlet area ratio of 1.27 and a mean rise angle of 28°. The inlet annulus height is 76.2 mm. The non-dimensional duct length (ITD axial length/inlet annulus height) is 3.4.

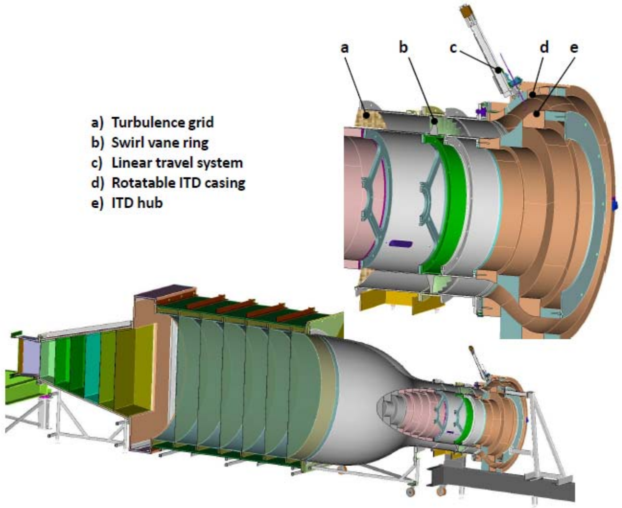

Figure 2. Annular test rig with changeable ITD test section

In the present experiment, an L-shaped seven-hole pressure probe with a tip diameter of 1.6 mm and a tip cone included angle of 30° was used for detailed 2D mapping measurements. The measurement grid in each plane consists of at least 31 points radially and 31 points circumferentially to cover one upstream swirl vane passage (7.5°). The ITD surface static pressure distributions were measured from static pressure taps along both the hub and casing. Surface oil flow visualization using a mixture of alkali refined linseed oil and titanium dioxide powder was also used to examine the flow behavior on both hub and casing surfaces.

The measurement locations in the ITD test section are shown in Figure 3. Location R is 300 mm upstream of the swirl vane ring and is used to provide tunnel operation reference as well as the boundary conditions for the numerical simulation. A linear traverse system can be mounted on the rotatable ITD casing to provide full area traversing at five different planes (A1 to A5). Location A1 is at the ITD inlet plane and Location A5 is at the ITD outlet plane. Three more traverse planes (A2, A3 and A4) were placed inside the duct and roughly perpendicular to both hub and casing surfaces. Figure 3 also gives the coordinate system, which was based on the local measurement plane.

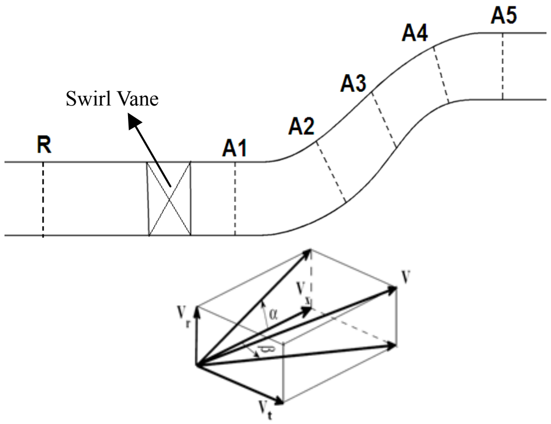

Figure 3. Measurement locations and coordinate system

All the pressure values are measured by using a Scanivalve DSA 3217 pressure scanner. The scanner has sixteen temperature compensated differential pressure transducers with a measurement range of ± 1250 Pa. The uncertainty in the measured pressure is estimated to be better than 0.05% of the transducer's full-scale range. The uncertainties in the measured dynamic and total pressures are estimated to be ± 0.5% and ± 0.25% respectively of the reference dynamic pressure. The Reynolds number, based on the height of the ITD inlet and the freestream velocity at location *R*, is 150,000 in all test cases.

The numerical simulation was performed using NUMECA Fine/Turbo 8.7.3. The detailed numerical setup can be found in Part I of this paper (Hu *et al.* [17]). The turbulent closure was achieved with *SST* (Shear Stress Transport) turbulence model. The inlet boundary condition for the simulations was established with measured profiles at location R. The outlet boundary condition was set as uniform atmospheric pressure. The grid topology consisted of approximately 3.17 million nodes, determined from a grid independence study, and y^+ was equal to or smaller than 2.

INLET FLOW CONDITION

In the current study, five vane rings with different swirl distributions were installed upstream the ITD to provided inlet wakes and swirl to the test section. The five swirl vanes can be classified into two sets. The design angles of the two sets of vane rings are summarized in Table 1. The first set, namely test cases A, B and C, has the same hub swirl angle of 20º, while the casing swirl angle are 20º, 30º and 40º, respectively. The second set, namely test cases D, B and E, has the same casing swirl angle of 30º, while the hub swirl angle are 10º, 20º and 30º, respectively.

Test Case	Hub Swirl	Casing Swirl	Mean Swirl	Swirl Gradient
A	20°	20°	20°	0°
B	20°	30°	25°	10°
C	20°	40°	30°	20°
D	10°	30°	20°	20°
B	20°	30°	25°	10°
E	30°	30°	30°	0°

Table 1. Summary of inlet swirl angles

Figure 4 presents the experimental and numerical pitchwise mass-averaged swirl angle, *β*, and total pressure coefficient, Cp_0, at the ITD inlet (Location A1) in test cases D, B and E (the second set). In Figure 4(a), both numerical and experimental results show that the deliberately designed hub swirl variation from 10º to 30º is clearly seen. In Figure 4(b), the pitchwise mass-averaged total pressure coefficient Cp_0 is almost identical in both CFD and experimental results which suggests that the ITD was tested under the same inlet conditions but different swirl angle distributions.

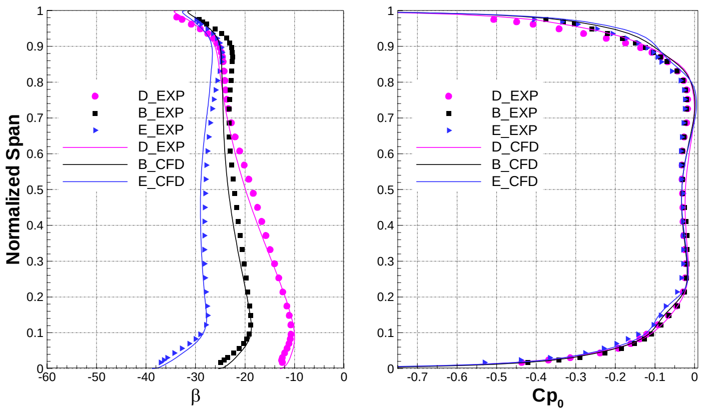

(a) Swirl angle **(b) Total pressure coefficient**

Figure 4. Pitchwise mass-averaged swirl angle *β* and total pressure coefficient Cp_0 at Location A1

RESULTS AND DISCUSSION

Influence of Hub Swirl Variation

Part I of the current study (Hu *et al.* [17]) showed that the *SST* turbulence model captured the flow physics in the current mild designed ITD reasonable well. Before the detailed flow developments in the ITD with different hub swirl angles in test cases D, B and E are discussed, the predicted pitchwise mass-averaged static pressure coefficient, Cp_s, within the ITD (top) and area-averaged static pressure coefficient, Cp_s, along ITD hub and casing (bottom) are presented in Figure 5. Additionally, the experimental results in case B are presented in Figure 5.

From Figure 5, both CFD and experimental results show a similar flow trend. Along the casing, there is a favorable pressure gradient before the first bend, followed by a strong adverse pressure gradient until the second bend and then a weak favorable pressure gradient to the exit. The strong adverse pressure gradient over a large portion of the casing may cause the boundary layer to separate. Along the hub, there is an adverse pressure gradient before the first bend and then the static pressure stays almost constant up to the second bend. There, a favorable pressure gradient is followed by the strong adverse pressure gradient. These two adverse pressure gradient regions may cause boundary layer separation at the hub as well. Additionally, the static pressure at the casing is lower at the first bend than that at the hub, while the opposite is true at the second bend, due to an increasing effective flow area and wall curvature. This static pressure difference between the hub and casing produces a radial pressure gradient, which tends to move fluid radially.

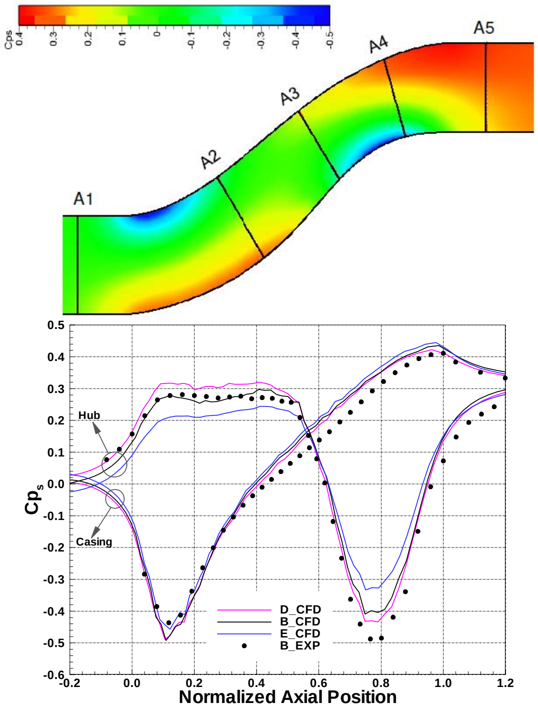

Figure 5. Static pressure coefficient Cp_s within ITD (top) and along hub and casing (bottom)

With the hub swirl angle increasing from 10º to 30º, the hub streamwise adverse pressure gradients both before the first bend and after the second bend are decreased. The higher inlet hub swirl angle results in a longer flow path through the ITD, thus reduces the effective flow curvature and decreases the streamwise pressure gradient correspondingly. The casing streamwise pressure gradient shows almost no difference in all three test cases. Furthermore, the radial pressure gradient is gradually increased at both the first and second bends of the ITD with decreasing hub swirl angle.

The predicted streamwise vorticity, $C_{\omega s}$, in the hub region of test case D, from swirl vane trailing edge (T.E.) to Location A2, are presented in Figure 6. Downstream of the swirl vane T.E., the hub region streamwise vorticity structures are dominated by the negative wake vorticity and the positive passage vorticity, labeled as *a* and *b* in Figure 6. These vorticity regions decrease at first (before Location A1) and then gradually grow as the flow convecting downstream through the first bend of ITD. As for the decrease in the magnitude of vorticity, this is due to the passage vorticity and wake vorticity dissipating downstream of the swirl vane. In the case of the increase in the vorticity magnitude, the detailed explanation will be presented next.

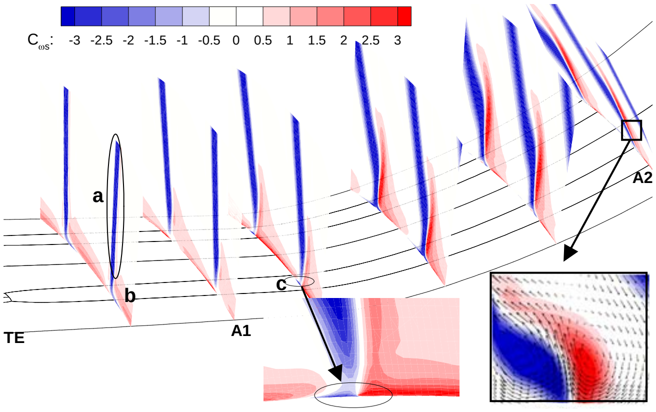

Figure 6. Predicted flood contour of streamwise vorticity coefficient $C_{\omega s}$ at hub region from T.E. to Location A2 in case D

After Location A1, as shown in Figure 5, the radial pressure gradient is from hub to casing. The low momentum wake flow and hub boundary layer, together with this radial pressure gradient will generate a pair of hub counter-rotating vortices, shown as region *c* in Figure 6. The initial hub counter-rotating vortices are starting rather small in size, and gradually increasing due to the strong radial pressure gradient. Then, the negative vorticity merges with the negative wake vorticity to form a single vortex, while the positive vorticity merges with the positive passage vorticity to form the other vortex. Therefore a pair of strong hub counter-rotating vortices is formed. The hub counter-rotating vortices continue to grow in strength, which can be observed through the increasing of the vorticity magnitude, as shown in Figure 6. Additionally, as seen in Figure 6, the direction of the hub counter-rotating vortices is also shown by the secondary velocity vectors which represent the deviation of the local velocity from the pitchwise mass-averaged velocity. It is observed that the hub low momentum flow had been radially moved into the hub counter-rotating vortices, which will make the hub boundary layer thinner.

The measured flood contour of total pressure coefficients, Cp_0, and streamwise vorticity coefficients, $C_{\omega s}$, from 2D mapping using the 7-hole pressure probe at different streamwise locations (A1 to A5) for test case D, B and E are presented in Figure 7. At ITD inlet (Location A1), the upstream wake and swirl distributions are shown by the total pressure deficit. The flow structures downstream of the swirl vane are dominated by the wake vorticity and the passage vorticity. Due to the inlet swirl gradient, the wake skew angle, which is the angle between the wake centre line and the vertical plane, is about 20°, 10° and 0°, in the counter-clockwise direction, in test cases D, B and E, respectively. As discussed in Part I of this paper (casing swirl variation), the magnitude of wake vorticity is higher with the larger swirl gradient. Therefore, test case D, with 20° inlet swirl gradient, has higher wake vorticity than the other two. The hub passage vorticity in test case E is strongest due to having the highest hub swirl angle. The casing vorticity is almost the same because of the same casing swirl angle. Comparing the total pressure magnitude in the three cases, it is found that they are almost the same at this location, which is desirable.

At Location A2, under the influence of the first bend radial pressure gradient, the strong hub counter-rotating vortices are detected in all three cases. The counter-rotating vortices are strongest in test case D and weakest in test case E. Firstly, this is because the upstream wake vorticity in test case D is the strongest, and the upstream wake vorticity in test case E is the weakest. The second reason for this is that the radial pressure gradient in test case D is the highest, while in test case E it is the lowest. The third possible reason is because of the hub 3D separation at the first bend predicted in test case D. This will be discussed later. Due to the effect of the hub counter-rotating vortices and the constant static pressure, the hub boundary layer thicknesses in all three cases are relatively thin. The hub boundary layer thickness in case E is the thickest due to the strong upstream passage vorticity effect and the weakest hub counter-rotating vortices. Additionally, the hub counter-rotating vortices are located at about 25% of the channel height and accumulate the hub region low momentum flow to form high loss cores in all the three test cases. Above these loss cores, the radial pressure gradient continuously drives the low momentum wake flow radially to feed into the casing boundary layer and weaken the wake. The 3D features of the casing boundary layer are not pronounced at this location, and only negative vorticity is detected in the casing region in all three cases. Furthermore, at Location A2 the wake is tilted in different ways in these three test cases. The wake skew angle is about 25° in a clockwise direction in case E, almost 0° in case B and 25° in a counter-clockwise direction in test case D. This is a result of the combined effects of the initial swirls, local curvature and angular momentum conservation, which tends to turn the wake clockwise at the first bend and counter-clockwise at the second bend. The detailed explanation of the wake tilt can be found in Part I of this paper (Hu *et al.* [17]).

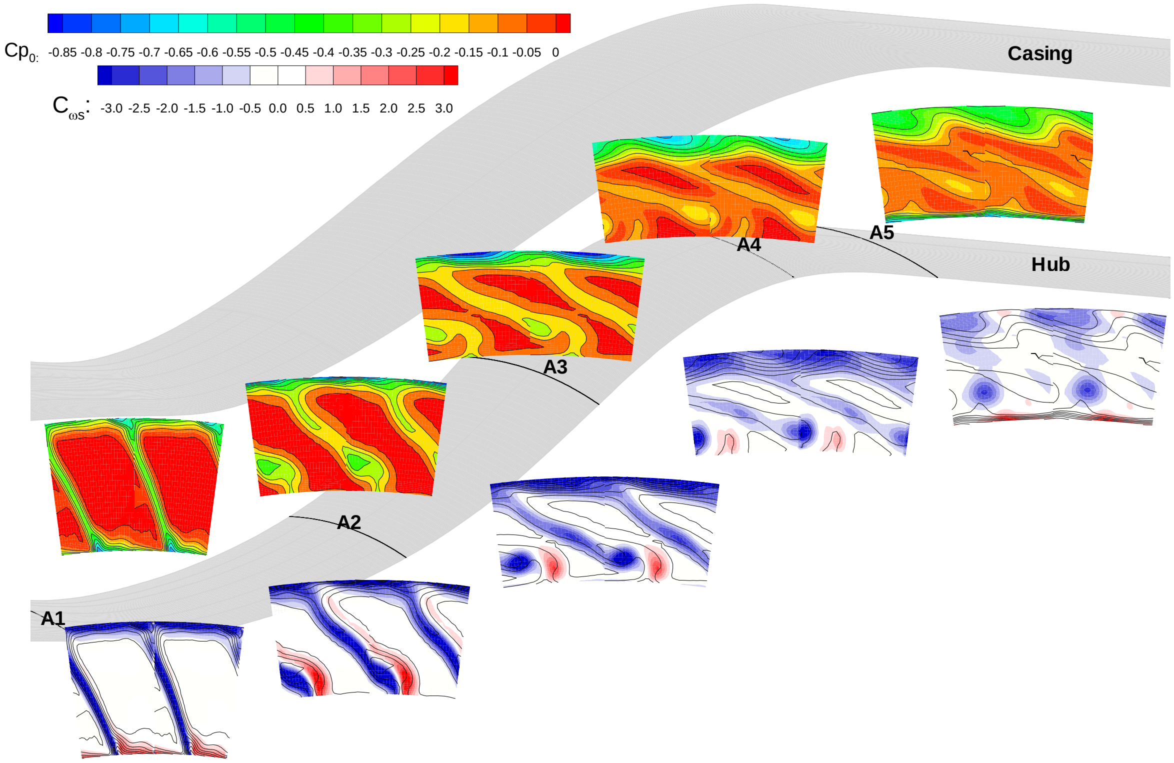

(a) Test case D (10°, 30°)

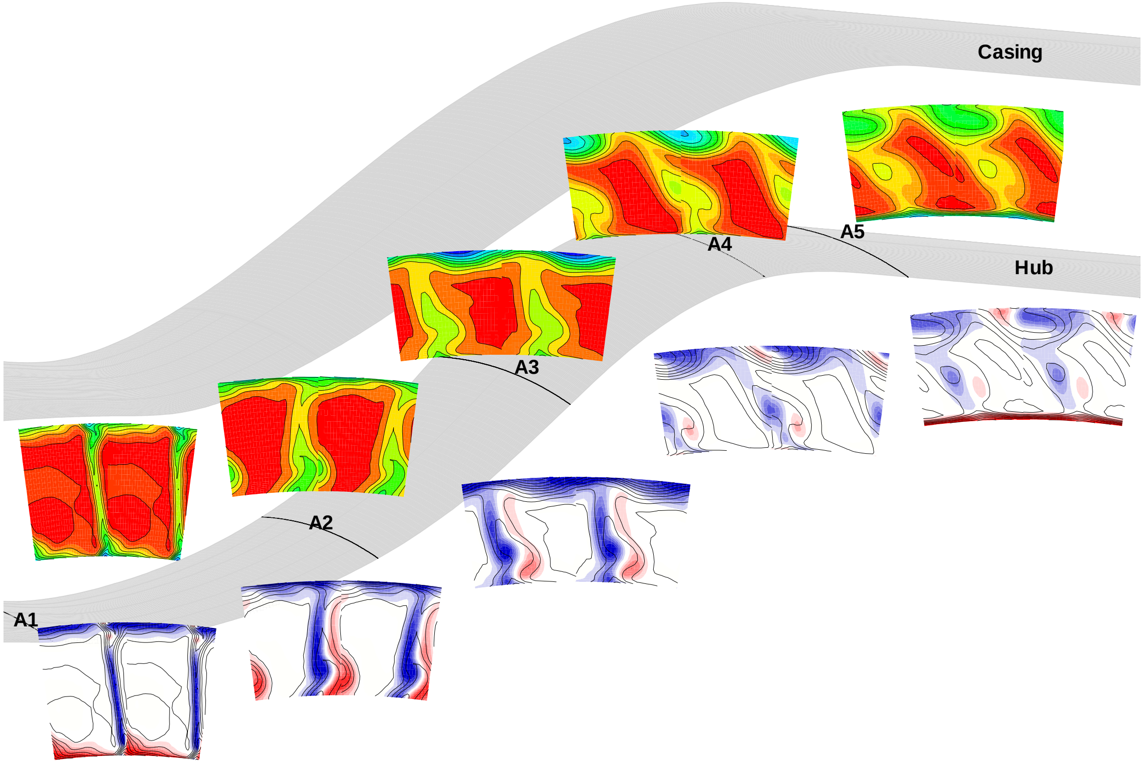

(b) Test case B (20°, 30°)

Figure 7. Measured total pressure coefficient Cp_0 and streamwise vorticity coefficient $C_{\omega s}$

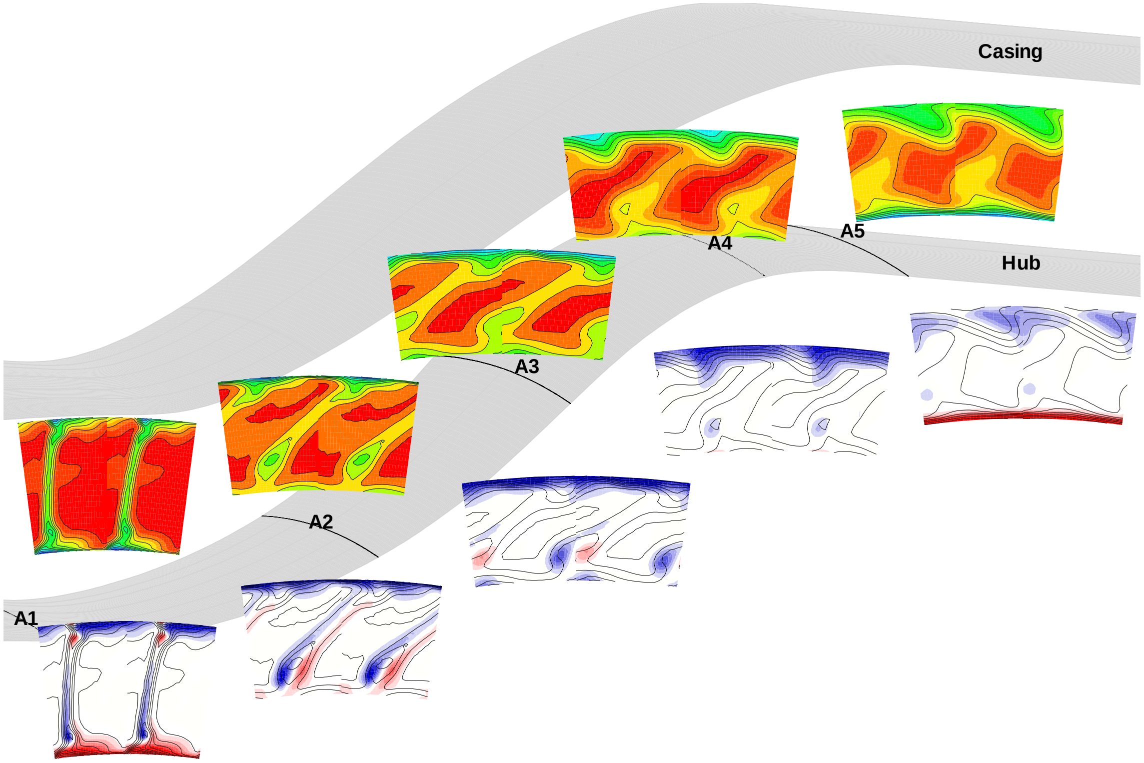

(c) Test case E (30°, 30°)

Figure 7. Measured total pressure coefficient *Cp_0* and streamwise vorticity coefficient *$C_{\omega s}$* (continued)

At Location A3, due to the upstream effect of the first bend radial pressure gradient, the hub counter-rotating vortices are moved away from the hub further, located at about 30% of the channel height. Comparing with that at Location A2, the strength of hub counter-rotating vortices is getting slightly weaker because of the low vortex dissipation rate. Furthermore, the vortex with the positive vorticity is dissipated much faster than the negative one. Since the positive vorticity produces a tangential velocity opposite to the mean flow tangential velocity, the tangential velocity in the positive vorticity region is reduced, which leads to increased vortex energy dissipation. On the other hand, the tangential velocity in the negative vorticity region is increased. Therefore, the pair of the counter-rotating vortices is shown slightly apart from each other because of the opposite tangential velocity for each of the vortices. The hub boundary layer thickness is still thin in test cases D and B. The hub boundary layer in test case E is thicker. The wake skew angle at this location is similar to that at Location A2. The low momentum wake flow above the hub vortices is fed into the casing boundary layer, forming a highly 3D casing boundary layer in both cases B and E. As described in Part I of this paper [17], the wake skew angle has a significant influence on the casing 3D boundary layer development. The large counter-clockwise wake skew angle in case D leads to less low momentum wake flow fed into the casing boundary layer, which causes weaker 3D features in the casing boundary layer. Additionally, only negative vorticity can be detected in the casing region in all test cases.

At Location A4, the radial pressure gradient is reversed as shown in Figure 5. The hub counter-rotating vortices become much weaker in all three test cases compared to those at Location A3. This is because the dissipation ratio for the hub counter-rotating vortices is much faster between Locations A3 and Location A4. The vortex with the positive vorticity is very weak in test cases D and B, and it has almost mixed-out in test case E. The hub boundary layer thickness in cases D and B is still thin due to the combined effects of the hub favorable streamwise pressure gradient and hub counter-rotating vortices. In case E, the hub boundary layer thickness is thicker than the other two cases, but it is thinner than that at Location A3 due to the effect of the hub favorable streamwise pressure gradient. Additionally, the hub boundary layer in case E is shown with strong 3D features due to the effect of the hub counter-rotating vortices. In the casing region, because of the 3D casing boundary layer and reversed radial pressure gradient, a pair of casing counter-rotating vortices is detected in case B. However, it is not formed in case E. This is because the radial pressure gradient at the second bend in test case E is lower, as shown in Figure 5. Additionally, due to the continual strong casing adverse pressure gradient and the 3D features of the casing boundary layer, a casing 3D boundary layer separation occurs between Locations A3 and

A4. The detailed discussion of the flow physics in the casing region can be found in Part I of this paper [17].

At Location A5, the hub counter-rotating vortices are still visible in cases B and D. They almost disappear in case E. From Locations A4 to A5, the vortices dissipation ratio is lower than that between Locations A3 and A4, because of the reduced second bend radial pressure gradient. The hub boundary layer thickness in all three cases is thicker than that at upstream locations because of the local adverse pressure gradient shown in Figure 5. The 3D features of the hub boundary layer are seen in all test cases. It is induced by the hub boundary layer 3D separation in cases B and D, while in case E it is due to the upstream hub boundary layer 3D feature from Location A4. This will be discussed further based on the hub surface flow visualization. With the effect of radial pressure gradient from casing to hub, the casing counter-rotating vortices are found in all three cases, the strongest occurring in case B, and the weakest occurring in case E.

To further investigate the hub swirl influence on the flow development, Figure 8 presents the hub flow visualizations, interpreted with the predicted wall shear stress vectors in the three test cases. The measurement locations, A2 to A5 are superimposed on flow visualization photograph of test case D.

Firstly, from Figure 8(a), in test case D, the predicted streamline captures the flow development along hub endwall reasonably well. The flow visualization presented clearly shows the accumulation of pigment as a thin low shear region on the ITD hub from the inlet to Location A4. In addition, there are two high shear stress regions on each side of the thin low shear stress region. This is caused by the strong hub counter-rotating vortices. After Location A4, a hub 3D separation is detected by a large low shear stress region. This hub 3D separation is caused by the strong adverse streamwise pressure gradient shown in Figure 5 at ITD exit. Correspondingly, from the predicted wall shear stress vectors presented in Figure 8(a), the same flow development is found. One convergence line begins from the inlet to Location A4 is detected, which is corresponding to the low shear stress region in flow visualization. It is seen that the hub boundary layer 3D separation occurs initially underneath the hub counter-rotating vortices. Furthermore, this separation is first seen in the positive vorticity part. This is because the positive vorticty produces a tangential velocity in the direction opposite to the flow swirl, which causes a slightly shorter flow path and a slightly stronger streamwise adverse pressure gradient. Additionally, as shown in Figure 8(a) in the rectangle, another hub 3D boundary layer separation at the first bend of ITD is found through the predicted wall shear stress vectors. This is due to the streamwise adverse pressure gradient in the first bend of ITD, as shown in Figure 5. This 3D separation at the first bend enhances the hub counter-rotating vortices.

As shown in Figure 8(b), for test case B, a pair of hub counter-rotating vortices, which are shown as a thin low shear region together with two narrow high shear strips on each side, and the hub 3D separation with low shear stress at the ITD exit are also found on the ITD hub endwall. From the details of predicted wall shear stress vectors, the convergence line is shown to have a longer path compared to that of the test case D due to the larger hub swirl angle. The hub 3D separation at the exit of the ITD is weaker than that in test case D because of the reduced adverse pressure gradient as shown in Figure 5. Additionally, as observed from the predicted wall shear stress vectors, there is no separation at the first bend of the ITD due to the reduced adverse pressure gradient as shown in Figure 5.

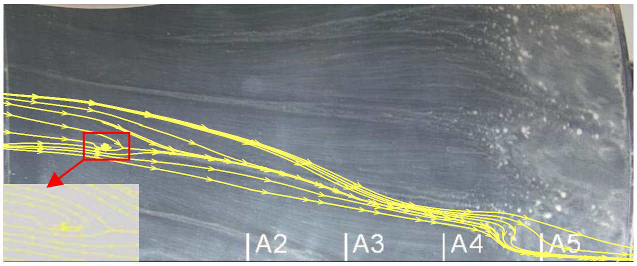

(a) Test case D (10^{o}, 30^{o})

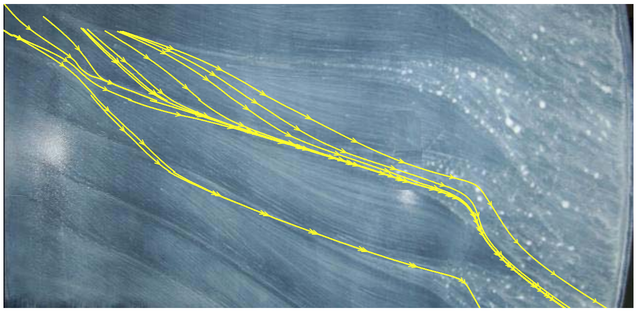

(b) Test case B (20^{o}, 30^{o})

(c) Test case E (30^{o}, 30^{o})

Figure 8. Hub flow visualizations interpreted with the predicted wall shear stress vectors

Regarding to the test case E of Figure 8(c), the flow visualization shows a thin low shear stress region together with two high shear stress regions detected in the first half of the ITD. Downstream of Location A3, it is difficult to detect the thin low shear region. This is because of the weak hub counter-rotating vortices in this case. Furthermore, at the exit of the ITD hub, a strong hub boundary layer separation with almost 2D features is detected. Correspondingly, from the predicted wall shear stress vectors, the convergence line is not as strong as those in cases D and B. The hub separation at exit of the ITD is also shown with 2D feature. The reason for the hub 2D separation is because the hub counter-rotating vortices in case E are the weakest and have almost disappeared by Location A5.

Consequently, from the analysis presented above, at the hub region, the radial movement of the low momentum hub boundary layer and wake flow induces a pair of hub counter-rotating vortices. This pair of counter-rotating vortices merges into the upstream vorticity, and forms a stronger pair of vortices, and persists until the ITD exit. The dissipation rate of hub counter-rotating vortices within the ITD is higher at the second bend due to the higher radial pressure from casing to hub. The positive part of the hub counter-rotating vortices contains a higher dissipation rate compared to the negative part. From a detail comparison of the three cases, the hub counter-rotating vortices are strongest when the inlet swirl gradient is the highest. The hub boundary layer thickness is the thickest as the inlet hub swirl angle is the largest. The hub 3D separation at both the first bend and the exit of the ITD are both reduced by the increased hub swirl angle. Additionally, the hub 3D separation at the exit of the ITD is influenced significantly by the hub counter-rotating vortices. In test case E, the hub boundary layer at exit is almost two-dimensional due to the weakest hub counter-rotating vortices.

Loss Mechanism within ITD

The flow physics discussed in the previous section regarding the variation of hub swirl, together with the study in Part I of this paper regarding the variation in casing swirl, show that the variations of the swirl distributions have a significant effect on both flow structures and loss distributions within the ITD. Therefore, the loss mechanisms through the ITD, due to different upstream swirl distributions, will be discussed in this section.

The measured mass-averaged total pressure loss coefficients, Y_p, of the ITD for the five test cases are presented in Table 2. The loss coefficientand, Y_p, is defined as,

$$Y_p = C_{P0,A5} - C_{P0,A1}$$

where $C_{P0,A1}$ and $C_{P0,A5}$ are the mass-averaged total pressure coefficient at Locations A1and A5, respectively. Comparing the results in Table 2, it is seen that the mass-averaged total pressure loss coefficient, Y_p, increases in the following order: test cases A, B, D, E and C. However, the differences in all loss coefficients, Y_p, for the five test cases are within 0.6%, which is not a significant different. Although the different inlet swirl distribution affects the flow development within ITD significantly as discussed previously, it does not result in large changes in the overall loss.

In order to examine the total pressure loss distribution through the ITD, Figure 9 presents the predicted mass-averaged total pressure loss coefficient Y_p through the ITD in the five test cases. The measurement locations (A1 to A5) are also shown in the figure. As shown in Figure 9, the total pressure loss coefficient Y_p at Location A5 is gradually increased from test case A, B, D, E to C. This is consistent with the measured results presented in Table 2.

Test Case	A	B	C	D	E
Y_p (%)	6.41	6.59	6.98	6.65	6.72

Table 2. Measured mass-averaged total pressure loss coefficient Y_p for five test cases

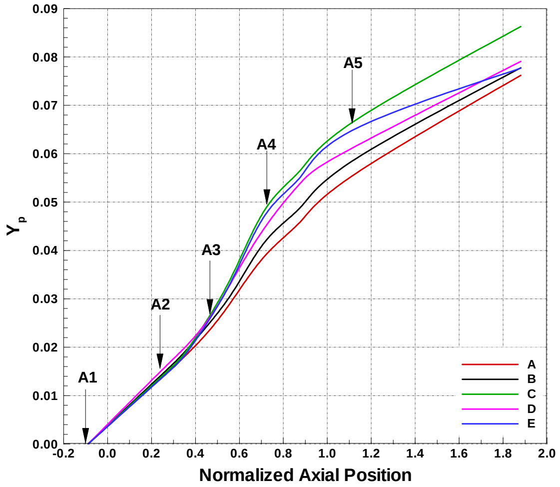

Figure 9. Predicted mass-averaged total pressure loss coefficient Y_p along ITD

From Location A1 to A3, the total pressure loss increases gradually. However, the total pressure loss shows very small differences among the five test cases. Based on the discussion before, the major flow characteristic in these regions is the strength of the hub counter-rotating vortices. It suggests that the hub counter-rotating vortices in this region is not a dominant loss source due to the very low vortex dissipation rate. From Location A3 to A4, the slopes of the curves, which represent the loss generation rate, for different test cases, increase rapidly in comparison with that from Location A1 to A3. The rapid dissipation of the hub counter-rotating vortices, together with the rapid growth of the casing boundary layer due to the adverse pressure gradient, cause the total pressure loss generation rate to increase rapidly. From Location A4 to A5, the slopes of the total pressure loss coefficient in all test cases are slightly flatter than those from Location A3 to A4. This is because the remainders of the hub counter-rotating vortices are weak and dissipate slowly. The casing boundary layer development is slowed slightly in this region due to the weak streamwise adverse pressure gradient. And the dissipation rate of casing counter-rotating vortices is also low. As the flow moves downstream from Location A5, all the slopes of the total pressure loss coefficients are reduced, especially in test case E. The casing boundary layer development, casing counter- rotating vortices dissipation and the remnant of the hub counter-rotating vortices are responsible for all the loss generation in this region. Since both the hub counter-rotating vortices and casing counter-rotating vortices are very weak in test case E, the loss generation rate in this case is much flatter than the others.

In order to characterize the radial loss distributions within the ITD, Figure 10 shows the experimental results of the pitchwise mass-averaged total pressure coefficient, Cp_0, at Location A5 with each of the different inlet swirl distributions. Two sets of the swirl angle distributions, *i.e.* casing variation (test cases A, B and C) in Figure 10(a) and hub variation (test cases D, B and E) in Figure 10(b), will be discussed separately. The radial Cp_0 profile is divided into four regions from hub to casing, namely the hub boundary layer dominant region, the hub counter-rotating vortices dominant region, the casing counter-rotating vortices dominant region and the casing boundary layer dominant region.

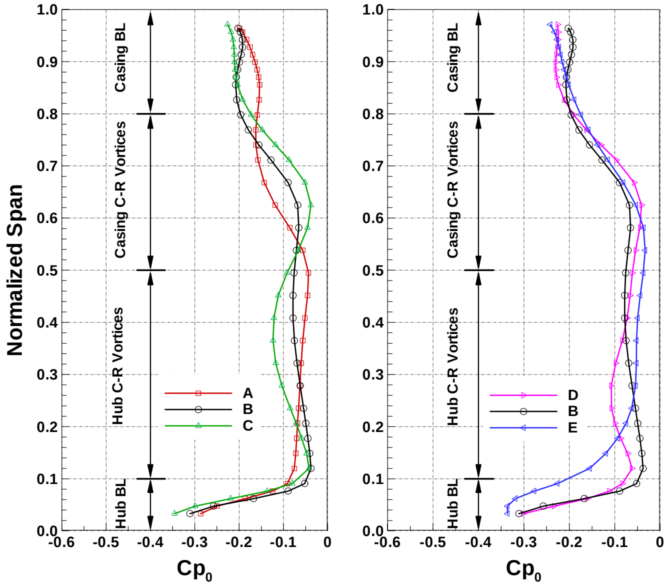

(a) 1st set (casing variation) **(b) 2nd set (hub variation)**

Figure 10. Measured pitchwise mass-averaged total pressure coefficient *Cp_0* at Location A5

Comparing from Figure 10(a), the total pressure coefficient in the casing boundary layer dominant region with that in the casing counter-rotating vortices dominant region, it is observed that the casing boundary layer loss is higher in all test cases. This suggests that the casing boundary layer loss is the primary loss contribution in the casing region of the ITD. The total pressure coefficient increases gradually from test case A, B to C in the casing boundary layer dominant region while it gradually decreases in the casing counter-rotating vortices dominant region. This is because the effects of the stronger casing counter-rotating vortices which scrape more low momentum casing boundary layer flow into the casing counter-rotating vortices dominant region and also delay the casing 3D boundary layer separation. Furthermore, since the hub counter-rotating vortices are gradually getting stronger from test cases A to B to C, the total pressure coefficient in the hub counter-rotating vortices dominant region is gradually increasing, as shown in Figure 10(a). However, the total pressure coefficient for the hub boundary layer dominant region is almost identical in all three cases due to having the same hub swirl angle. As discussed above, the hub boundary layer thickness is rapidly increasing near the exit of the ITD due to the strong streamwise adverse pressure gradient. In this region, the hub counter-rotating vortices are too weak to affect hub boundary layer development.

As shown in Figure 10(b), with the constant casing swirl angle, there is no significant difference in the casing region. With the relatively stronger casing counter-rotating vortices of test case B, the total pressure loss is relatively small in the casing boundary layer dominant region, and is relatively large in the casing counter rotating vortices dominant part. With the gradually decreasing strength of the hub counter-rotating vortices from test cases D to B to E, the loss in hub counter-rotating vortices dominant region gradually decreases. Additionally, in the hub boundary layer dominant region, the total pressure loss for the test case E is the largest among the three test cases. This is primarily due to the thickest hub boundary layer, the strongest upstream passage vorticity and the weakest upstream hub counter-rotating vortices, as mentioned before.

CONCLUSIONS

The aim of the current study was to investigate the influence of the inlet swirl distributions on the flow development and loss mechanism within an S-shaped ITD. Two sets of inlet swirl distributions, i.e. casing swirl variation and hub swirl variation, are studied separately. This paper is the second part of the current study and investigates the effects of the hub variation on the flow physics within the ITD.

The radial movement of the hub boundary layer and wake low momentum flow induces a pair of hub counter-rotating vortices. This pair of counter-rotating vortices merges into the upstream vorticity, forms a stronger pair of vortices, and persists up to the ITD exit. The dissipation rate of the hub counter-rotating vortices within the ITD is higher at the second bend due to the higher radial pressure from casing to hub. Furthermore, the positive part of the hub counter-rotating vortices has a higher dissipation rate compared with the negative part. From a detailed comparison among the three test cases, the hub counter-rotating vortices are the strongest as the inlet swirl gradient is the largest. The hub boundary layer thickness is the thickest as the inlet hub swirl angle is the greatest. The hub 3D separation occurring at the exit of the ITD is reduced with an increase in the hub swirl angle. Additionally, the hub 3D separation is significantly influenced by the hub counter-rotating vortices that trend to be two-dimensional in the case with the weakest hub counter-rotating vortices.

Based on the study in both parts of this paper, a detailed loss mechanism has been described. Within an ITD with smaller boundary layer separations, the loss at the first bend is not pronounced, while it increases rapidly at the second bend due to the high dissipation rate of hub counter-rotating vortices and rapid casing boundary layer development. After the second bend, the casing boundary layer development is the dominant loss source. Furthermore, the losses within the ITD are significantly redistributed by the hub and casing counter-rotating vortices. The stronger the casing counter-rotating vortices, the larger the loss in the casing counter-rotating vortices dominant part, and the smaller the loss in the casing boundary layer dominant part. The weakest hub counter-rotating vortices induce the smallest loss at hub counter-rotating vortices dominant region but the highest loss in the hub boundary layer dominant region. Therefore, for the design of an ITD with mild parameters, it is better to have smaller upstream swirl gradient and smaller mean swirl.

The loss analysis in this paper is based on the study of an ITD with relatively small separations. Detailed investigation on the loss development in more aggressive ITDs will be presented in the future work.

ACKNOWLEDGMENTS

The authors wish to acknowledge the financial support of the National Research Council of Canada and Pratt & Whitney Canada. The technical support from Dr. Michael Benner, Dr. Ali Mahallati and Mr. Paul Hunt is greatly appreciated.

NOMENCLATURE

Cp_0	total pressure coefficient
Y_p	ITD total pressure loss coefficient
P_0	total pressure
Cp_s	static pressure coefficient
$C_{\omega s}$	normalized streamwise vorticity ω_s by $U_{ref}/\Delta R$
SST	Shear Stress Transport
x	axial coordinate
r	radial coordinate
t	tangential coordinate
U_{ref}	velocity at Location R
V_x	axial velocity
V_t	tangential velocity
V_r	radial velocity
β^o	swirl angle $=\tan^{-1}(V_t/V_x)$
α^o	radial angle$=\tan^{-1}(V_r/V_x)$
ΔR	the annulus height at the ITD inlet
ω_x	axial vorticity
ω_t	tangential vorticity
ω_r	radial vorticity
ω_s	streamwise vorticity

REFERENCES

[1] Hu, S. Z., Zhang, X. F., Benner, M., Gostelow, P. and Vlasic, E., 2010, “Geometric Optimization of Aggressive Inter-turbine duct", ASME 14th International Mechanical Engineering Congress & Exposition, IMECE 2010-37323.

[2] Bradshaw, P., 1976,“Effects of Steamline Curvature on Turbulent Flow”, AGARD-AG-169.

[3] Lohmann, R. P., Markowski, S. J., and Brookman, E. T., 1979, “Swirling Flow Through Annular Diffusers with Conical Walls”, ASME J. Turbomach, Vol 101, pp. 224-228

[4] Kumart, D. S., and Kumart, K. L., 1980, “ Effect of Swirl on Pressure Recovery in Annular Diffusers ”, Journal Mechanical Engineering Science, Vol 22, No.6, pp. 305-313

[5] Miller, R. J., Moss, R. W., Ainsworth, R. W., and Harvey, N. W., 2003, “The Development of Turbine Exit flow in a Swan-Necked Inter-Stage Diffuser”, ASME Paper GT2003-38174.

[6] Miller, R. J., Moss, R. W., Ainsworth, R. W., and Harvey, N. W., 2004, “The Effect of an Upstream Turbine on a Low-Aspect Ratio Vane”, ASME Paper GT2004-54017.

[7] Marn A., Göttlich E., Pecnik R., Malzacher F. J., Schennach O. and Pirker H. P., 2007, “The Influence of Blade Tip Gap Variation on The Flow Through an Aggressive S-Shaped Intermediate Turbine Duct Downstream of a Transonic Turbine Stage – Part I: Time-Averaged Results”, ASME Paper GT2007-27405.

[8] Göttlich E., Marn A., Pecnik R., Malzacher F. J., Schennach O. and Pirker H. P., 2007, “The influence of blade tip gap variation on the flow through an aggressive S-shaped intermediate turbine duct downstream of a transonic turbine stage – Part Π: Time-averaged results and surface flow”, ASME Paper GT2007-28069.

[9] Marn, A., Göttlich, E., Malzacher F. and Pirker, H.P., 2009, “The Effect of Rotor Tip Clearance Size onto the Separation Flow Though a Super-Aggressive S-shaped Intermediate Turbine Duct Downstream of a Transonic Turbine Stage”, ASME Paper GT2009-59934.

[10] Dominy, R. G., and Kirkham, D. A., 1995, “The Influence of Swirl on the Performance of Inter-Turbine Diffusers”, VDI Berichte 1186, pp. 107-122.

[11] Dominy, R. G., and Kirkham, D. A., 1996, “The Influence of Blade Wakes on the Performance of Inter-Turbine Diffusers”, ASME J. Turbomach, Vol 118, pp. 347-352.

[12] Dominy, R. G., Kirkham, D. A., and Smith A. D., 1998, “Flow Development Through Inter-turbine Diffusers”, ASME J. Turbomach., Vol 120, pp. 298-304.

[13] Bailey. D. W., and Carrotte, J. F., 1996, “ The Influence of Inlet Swirl on the Flow within an Annlar S-Shaped Duct”, ASME Paper 96-GT-60.

[14] Axelsson L.-U., Arroyo Osso C., Cadrecha D. and Johansson T. G., 2007, “Design, Performance Evaluation and Endwall Flow Structure Investigation of an S-shaped Intermediate Turbine Duct”, ASME Paper GT2007-27650.

[15] Axelsson, L.-U. and Johansson, T.G., 2008, “Experimental Investigation of the Time-Averaged Flow in an Intermediate Turbine Duct”, ASME Paper GT2008-50829.

[16] Zhang, X. F., Hu, S. Z., Benner, M., Gostelow, P. and Vlasic, E., 2010, “Experimental and Numerical Study on an Inter-turbine Duct", ASME 14th International Mechanical Engineering Congress & Exposition, IMECE 2010-37322.

[17] Hu, S. Z., Zhang, Y. F., Zhang, X. F. and Vlasic, E., 2011, “Influnence of Inlet Swirl Distributions on an Inter-Turbine Duct- Part I: Casing Swirl Variation”, ASME Paper, IGTI GT2011-45554.

[18] Yaras, M. and Sjolander, S.A., 1990, “Development of the Tip-Leakage Flow Downstream of a Planar Cascade of Turbine Blades: Vorticity Field”, ASME Paper 1990, Vol 112, 610-617.